

# Elasto-frictional reduced model of a cyclically sheared container filled with particles

Antoine Faulconnier<sup>1,2</sup>, Stéphane Job<sup>1\*</sup>, Julien Brocaïl<sup>2</sup>, Nicolas Peyret<sup>1</sup>  
and Jean-Luc Dion<sup>1</sup>

<sup>1</sup>Laboratoire Quartz (EA-7393), ISAE-Supméca, 3 rue Fernand Hainaut,  
Saint-Ouen-sur-Seine, 93400, France.

<sup>2</sup>Estaca'Lab, Estaca campus Ouest, rue Georges Charpak, Laval, 53000, France.

\*Corresponding author(s). E-mail(s): [stephane.job@isae-supmeca.fr](mailto:stephane.job@isae-supmeca.fr);

## Abstract

This article explores the hysteretic behavior and the damping features of sheared granular media using discrete element method (DEM) simulations. We consider polydisperse non-cohesive frictional spherical particles, enclosed in a container with rigid but moving walls, submitted to a cyclic simple shear superimposed to a confining pressure. The mechanical response of the grains is analyzed in the permanent regime, by fitting the macroscopic stress-strain relation applied to the box with a Dahl-like elasto-frictional model. The influence of several parameters such as the amplitude of the strain, the confining pressure, the elasticity, the friction coefficient, the size and the number of particles are explored. We find that the fitted parameters of our macroscopic Ansatz qualitatively rely on both a well-established effective medium theory of confined granular media and a well-documented rheology of granular flow. Quantitatively, we demonstrate that the single degree-of-freedom elasto-frictional reduced model reliably describes the nonlinear response of the granular layer over a wide range of operating conditions. In particular, we show that the mechanical response of a granular slab under simple shear depends on an unique dimensionless parameter, akin to an effective Coulomb threshold, at low shear/high pressure. Further, exploring higher shear/lower pressure, we evidence an optimal damping at the crossover between a loose unjammed regime and a dense elastic regime.

## Date

December 10, 2024

## 1 Introduction

Granular materials are ubiquitous in Nature, where they are found in a variety of states of matter [1]. From the application point of view, granular media are known to dissipate and disperse efficiently mechanical shocks (*a sand pile can stop a rifle bullet*) and they proved to be efficient also in the context of sound and vibration mitigation [2], damping [3] and insulation [4].

Compared to classical matter, granular media present unusual properties like softening [5], weakening [6], phase transition [7] relaxation [8] and aging [9], to name but a few.

Jammed granular media are frequently referred to as granular solids owing to their ability to resist to pressure and shear, or even as metamaterials [10] to tailor wave absorption [11] and propagation [12]. To determine their elastic

features, an effective medium theory (EMT) was developed in the late 80's to connect the elastic moduli at the particle level to the one at the sample scale [13]. Such a macroscopic description of a pile of grains inherit and reveal the intrinsically nonlinear Hertzian potential at the heart of the contacts mechanics [14, 15]. When the particles are non-cohesive and dry, they are likely submitted also to friction [15]. Frictional properties are particularly studied in the field of granular flow, in line with many industrial applications, where one of the bottleneck relies on understanding how friction dictates the rheology of an avalanche, for instance [16]. Here, a key description is found in dense and slow granular flows, where such a behavior can be described with the tools and definitions of soil mechanics [17–19]. In this context, an effective friction coefficient is defined as the ratio between shear stress and confining pressure [16]. Interestingly, this macroscopic coefficient only depends on a dimensionless inertial number  $I$  [20, 21].

Inter-particle friction, together with inelastic collisions between grains, is also a key feature to damp mechanical energy in discrete systems. Indeed, vibrated granular media are able to achieve perfectly inelastic collapse conditions [22, 23], leading to exceptional damping efficiency [3, 24–26]. Here, the dry friction being mostly a frequency independent mechanism, it is much more effective at low frequency than the viscoelastic damping [27, 28]. Phenomenologically, the friction between numerous particles gives rise to powerful hysteretic behaviors at the sample scale [8, 29], which themselves rely on multiple stick-slip events at the contact scale, leading in practice to nonlinear damping properties [30–33]. The macroscopic hysteretic response is thus closely related to the anisotropy and the topological disorder of the contact network, as evidenced for instance by X-Ray tomography of granular media under shear [34].

In the vast majority of the studies on granular media, simulations based on discrete element method (DEM) are widely used to model soils [35, 36] and structure made of particles [37, 38] to explore in-depth phenomena at the microscopic scale; such a detailed description generally remains a challenging task in experiments, due to the large number of interacting bodies. For instance, Luding *et al* [39, 40] used DEM simulations in order to build a constitutive model

describing the behavior of a bi-axial box filled with particles submitted to pure shear in two-dimensions [39], by taking into account for various phenomena like anisotropy, hysteresis and ratcheting. This model was later enriched to include pressure relaxation and stabilization in pure shear [40], allowing to describe transient as well as permanent regimes. Other extensive models for granular matter include granular solid hydrodynamics [41] handling static behavior with plasticity, but also transient loading [42] including hysteresis.

From the practical engineering point of view, models were also derived to describe the macroscopic mechanical response of structural elements, such as a slender composite beam containing a granular medium core, from either simulations [10] or experiments [43]. In line with these attempts, our study aims at deriving a simplified but reliable description of a vibrated confined granular medium, capable of reducing the complexity of DEM simulations in order to facilitate, for instance, the optimization of vibrations dampers containing particles [44]. In particular, we require our reduced model to be parametrized by identifiable and measurable quantities, such as the features of the grains (size, material, ...) and the features of the mechanical driving (confinement pressure, shear amplitude, ...). Starting from a DEM numerical model of individual grains confined in a box and submitted to cyclic simple shear, we thus provide and analyze, in this study, an elasto-hysteretic reduced model at the macroscopic scale. The evolution of the elastic as well as the damping features of both the numerical model and the reduced model are explored, seeking in particular for configurations with high damping ratio.

The paper is organized as follows. The Sec. 2 describes the setup of the DEM simulation to model a pack of grains enclosed in a box undergoing simple shear cyclically. In Sec. 3, the evolution of quantities of interest such as the shear stress, the pressure, the elasticity and frictional behaviors are identified and examined at the light of an elasto-hysteretic Ansatz made of a hysteretic term rendered by Dahl model, combined to a linear elastic response. the reliability of this model is probed via an extensive parametric study. In Sec. 4, we evidence how our Ansatz relates to an effective medium theory describing the macroscopic elasticity of granular media, and to a

rheological model describing granular flows. Further, we find through a dimensional analysis that the granular material can be described reasonably by a single non-dimensional parameter, akin to an effective Coulomb threshold. The reliability of this model is discussed and then used to estimate the damping features. Finally, we propose a non-linear improvement of the model, stemming from the anisotropy-like pressure fluctuations observed at high shear/low pressure; these fluctuations are described by a second non-dimensional parameter. The Sec. 5 is the conclusion.

## 2 Method and protocol

We build a numerical version of a granular medium with a lateral size that is large enough compared to the average particle radius, in order to get rid of the discreteness of the medium at the scale of the representative elementary volume. Our numerical sample thus consists of 1000 ( $10 \times 10 \times 10$ ) polydisperse and purely elastic spherical particles (nominally made of steel: mass density  $\rho_p = 7850 \text{ kg/m}^3$ , Young's modulus  $E_p = 210 \text{ GPa}$ , Poisson ratio  $\nu_p = 0.27$ , inter-particle friction coefficient  $\mu_p = 0.15$ ), with uniformly distributed radii to prevent crystallization ( $r_p = 1 \pm 0.25 \text{ mm}$ ). Grains are placed within a cubic box with rigid but movable walls. The model is simulated using DEM with *Yade* [45] open source software. For this, Newton's equations of motion are integrated in the time domain with an explicit second order Velocity Verlet scheme, with a constant time step chosen equal to the time of flight of the longitudinal waves across the smallest particle,  $\Delta t = \min(r_p/\sqrt{M_p/\rho_p})$ , being  $M_p = E_p(1 - \nu_p)/(1 + \nu_p)(1 - 2\nu_p)$  the P-wave modulus of particles material. This time step is always smaller than the duration of inter-particle mechanical contact (i.e. the smallest duration in the system) because the deformation rate is smaller than the P-wave speed [14, 15]; this choice thus ensures a proper discretization in time to fulfill energy conservation. Elasto-frictional interactions between particles are described by Hertz-Mindlin contact law coupled with a Mohr-Coulomb criterion, which means that the normal and the tangential contact forces  $F_{n,t}$  versus deformations  $\delta_{n,t}$  take the

form [14, 15]

$$F_n = \frac{2}{3}k_n r_p^{1/2} \delta_n^{3/2} \text{ with } k_n = \frac{2E_p}{1 - \nu_p^2}, \quad (1)$$

$$F_t = k_t (r_p \delta_n)^{1/2} \delta_t \text{ with } k_t = \frac{8G_p}{2 - \nu_p}, \quad (2)$$

if the particles overlap due to compression and stick due to friction; otherwise, both forces tend to zero when the non-cohesive particles do not overlap,  $\delta_n \leq 0$ , and the tangential force saturates if sliding occurs,  $F_t = \min(\|F_t\|, \mu_p F_n) \times \text{sign}(\dot{\delta}_t)$ . Here,  $G_p = E_p/2(1 + \nu_p)$  is the shear modulus of the particles material and  $k_{n,t}$  are their normal and tangential contact stiffnesses. Without loss of generality, the particle-to-wall interactions are chosen frictionless ( $\mu_w = 0$ ). This choice implies that no shear stress occurs between the particles and the walls in any directions, and simplifies the interpretation on the origin of the dissipation which, in this case, only comes from inter-particle friction. This approximation is supported by the fact that the particle-to-wall contacts are far less numerous than the particle-to-particle ones, they introduce a negligible correction in the macroscopic mechanical response.

In a *first step*, we prepare a granular sample. We generate the 1000 size-distributed particles placed at random positions in a dilute state (at rest and well separated), inside a large cubic box delimited by walls, using an *Yade*'s builtin generator. Then, we set the sample under pressure, by proceeding with an isotropic compression until a given volume fraction  $\phi = V_p/V$  is reached, with  $V_p$  the material volume of the spheres and  $V$  the volume of the parallelepiped box. This step is achieved by imposing the displacement of all the walls at a constant and slow normal velocity, see Fig. 1 (top-left); note the walls do not interact with each other.

In a *second step*, the granular packing is submitted to cyclic simple shear. In practice, the box is deformed by imposing the rotation of two of the side walls, see Fig. 1 (top-right), similarly to what was done experimentally in [34]. However, in our case, the volume of the box is kept constant, whereas the confining pressure is kept constant in [34]. We impose an harmonic rotation angle  $\theta(t) = \theta_m \sin(\omega_0 t)$  leading to a shear strain  $\gamma = \tan(\theta)$  which is quasi-harmonic in the limit of

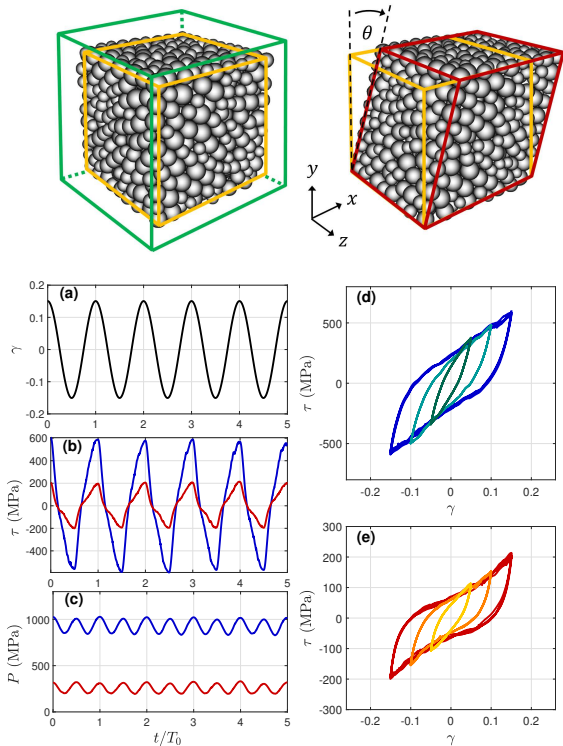


**Fig. 1** (top) Granular sample during (left) initial compression and (right) cyclic shear. (a) Imposed shear strain, (b) shear stress and (c) hydrostatic pressure, as functions of time for two values of the volume fraction  $\phi = 0.64$  (red) and  $\phi = 0.70$  (blue) at  $\gamma_m = 0.15$ . Stress-strain curves for (d)  $\phi = 0.70$  and (e)  $\phi = 0.64$  at various amplitude:  $\gamma_m = 0.05, 0.10$  and  $0.15$ .

small angles,  $\gamma(t) \simeq \gamma_m \sin(\omega_0 t)$  with  $\gamma_m \simeq \theta_m \ll 1$ . It is important to note that, here and in the following, cyclic shear transformations are quasi-static in order to neglect inertia in the forces and moments balance. The latter condition is  $\omega_0 t_w \ll 1$  in practice, the angular frequency being proportional to the shear rate,  $\omega_0 \propto \dot{\gamma}$ , and the time of flight of a compressional wave across the granular medium being  $t_w = r_p / \sqrt{M_{\text{eff}} / \rho_{\text{eff}}}$ , with  $\rho_{\text{eff}} \propto \rho_p$  the mass density and  $M_{\text{eff}} = K_{\text{eff}} + (4/3)G_{\text{eff}}$  the longitudinal modulus of the sample's effective medium defined in Sec. 4.1 below.

The DEM computation allows extracting the instantaneous quantities at the contact scale from which we compute the variables of interests and the state variables as functions of time: namely, the shear strain  $\gamma(t)$ , the shear stress  $\tau(t)$ , the hydrostatic pressure  $P(t)$ , the average coordination number  $Z(t)$ , and the volume fraction

$\phi(t) = \text{const}$  (maintained constant during the simple shear transformation). The pressure in the granular medium is estimated as the trace of the stress tensor  $P = (\sigma_{xx} + \sigma_{yy} + \sigma_{zz})/3$ , where  $\sigma_{ii} = (\mathbf{F}_{+i} \cdot \mathbf{n}_{+i} + \mathbf{F}_{-i} \cdot \mathbf{n}_{-i})/2S_i$  with  $S_i$  the area of face  $i = (x, y, z)$ , is computed from the total forces  $\mathbf{F}_{\pm i}$  exerted by the particles on the faces defined by their normal vectors  $\mathbf{n}_{\pm i}$ . We checked that this estimation of the confining pressure is consistent, by less than 0.1% relative difference, with the one computed from the trace of the Love-Weber stress tensor [45–47]. The onset of jamming [48] (which corresponds to the onset of a pressure in the sample, at which it gets an elasticity) is reached at around a volume fraction  $\phi_c = 0.595 \pm 0.003$  (0.5%) in average [49, p.111], over all the dataset presented in this study. The shear stress  $\tau$  is computed by summing all the reactions applied by the particles on the side walls, which are equivalent to two resisting moments computed at the center of rotation of the walls. The moments  $\mathbf{M}_{+x}^{Oz}$  and  $\mathbf{M}_{-x}^{Oz}$ , exerted on the two opposite faces  $\mathbf{n}_{\pm x}$ , are used to compute the magnitude of an equivalent shear stress  $\tau = -2(\mathbf{M}_{+x}^{Oz} \cdot \mathbf{z} + \mathbf{M}_{-x}^{Oz} \cdot \mathbf{z})/V$  exerted in-plane on the top wall  $\mathbf{n}_{+z}$ , where  $\mathbf{z}$  is the cartesian vector. Here as a crude check, we verify that the work done by the shear force (the injected energy) equals the total energy per unit volume in the granular medium computed by the DEM,  $\int \tau d\gamma = e$ .

## 3 Results

### 3.1 Evolution of the shear stress

Once the sample is set under pressure at a given packing fraction, a quasi-harmonic simple shear strain shown in Fig. 1a is imposed to it as described in Sec. 2. The data on Fig. 1b present the evolution of the shear stress reaction between the walls of the container and the granular sample to accommodate such a motion, for two examples, at packing fraction  $\phi = 0.64$  and  $\phi = 0.70$ . At such confinements, the average strain of the contacts [50] is  $\langle h/a \rangle \approx 0.02$  and  $\langle h/a \rangle \approx 0.04$ , respectively, see the Fig. A1 in the Appendix Sec. A1. In both cases, a nonlinear response is clearly evidenced in the stress-strain relation  $\tau(\gamma)$ , see Figs. 1d and 1e. Indeed, we observe an hysteretic behavior on Fig. 1d at  $\phi = 0.70$ , with a noticeable dependence with the shear amplitude

$\gamma_m$ . For instance, following clockwise the evolution of the stress-strain curve  $\tau(\gamma)$  with the largest amplitude, shown as the darkest blue curve on Fig. 1d, starting from the left-bottom cusp point at  $\gamma(t) = -0.15$ , we can see that after a nonlinear growth,  $\tau$  reaches a saturating point where it starts to increase linearly with respect to  $\gamma$ . Then  $\tau$  reaches the right-top cusp point at  $\gamma(t) = 0.15$  before pursuing the same track backward. The behavior at  $(\phi, \gamma_m) = (0.70, 0.15)$  has to be contrasted to the one at  $(\phi, \gamma_m) = (0.64, 0.15)$  presented on Fig. 1e, see the darkest red curve: the stress-strain curve follows a similar trend, except that the linear growth before reaching cusp points becomes even more nonlinear, with an additional stiffening inflection. Such an inflection is less obvious in the case  $(\phi, \gamma_m) = (0.64, 0.10)$  seen on Fig. 1e, for which the hysteresis curves appear more similar to the one at  $(\phi, \gamma_m) = (0.70, 0.15)$ . Also in both cases seen on Figs. 1d and 1e, the hysteresis tend to shrink and transform into a linear elastic response at the smallest amplitudes.

All these observations thus highlight a symmetry of the roles played by the packing fraction, the confinement pressure and the shear strain amplitude on the mechanical response of the granular sample: large packing fractions, large confinement pressures and small strain amplitudes tend to linearize the stress-strain relation. This feature will be further discussed and exploited in more details in the following sections.

### 3.2 Evolution of the pressure

The evolution of the pressure during cyclic shear is plotted on Fig. 1c. It shows that the pressure is fluctuating even though the cyclic shear transformation is isochoric. This phenomenon has the same origin as the so-called Reynolds dilatancy, an usual fluctuation of the volume fraction  $\phi$  when the shear transformation is performed at constant pressure, as for instance in [34]. In the later case, the granular medium has the tendency to expand when submitted to shear strain. In the case where the volume is constrained, the volume fraction is prescribed, the dilatancy is thus frustrated, which results in a fluctuation of the pressure. This variation, called the *Reynolds pressure* in [8], can be described as

$$\tilde{P}(t) = P + \delta P(t) = P_0 + R\gamma^2(t), \quad (3)$$

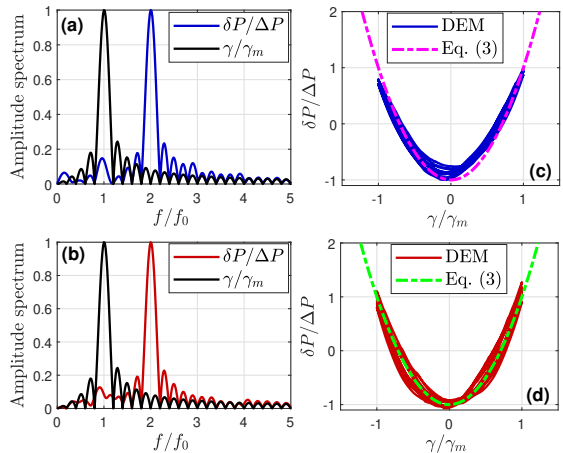


**Fig. 2** (a,b) Spectra of the shear strain and the pressure fluctuation and (c,d) pressure fluctuation as a function of the shear strain, for the two examples shown in Fig. 1: (a,c)  $\phi = 0.70$  and (b,d)  $\phi = 0.64$ , both at  $\gamma_m = 0.15$ . Data in (c,d) are compared to a quadratic behavior, with (c)  $R = 7.54$  GPa and (d)  $R = 4.49$  GPa, where  $\Delta P = R\gamma_m^2/2$  is the peak amplitude of the pressure fluctuations, see Eq. 3.

where  $P$ ,  $P_0$  and  $\delta P$  correspond to the time average, the static value and the fluctuation of the pressure, respectively. Because of the quadratic dependency in shear deformation, the static pressure  $P_0$  (i.e. the pressure at zero strain,  $\gamma_m = 0$ ) and the mean pressure  $P = P_0 + \langle R\gamma^2 \rangle$  are not equal; however, they remain close for small strain amplitudes,  $R\gamma_m^2 \ll P$ . The *Reynolds coefficient*  $R$  was first introduced by Ren *et al* in [8], where it was demonstrated to be related to the volume fraction,  $R = A(\phi_c - \phi)^n$  with  $n \simeq -3.3$  for cylindrical particles in 2D and  $A$  having the dimension of an elasticity. It is worth pointing out that the behavior of  $R$  was examined below jamming in [8],  $\phi < \phi_c$ , while our study is conducted in a 3D packing of spherical grains above jamming,  $\phi > \phi_c$ , which is likely to provide a different scaling of  $R$  with respect to the packing fraction. In our case, we find that  $R \propto (\phi - \phi_c)^n$  with  $n \simeq 0.56$ , see Fig. A2a in the Appendix Sec. A2. In an alternative manner, a dependency of the pressure  $P$  with the shear strain  $\gamma$  was also captured by the constitutive model derived by Luding *et al* in [40], which demonstrates that the pressure fluctuations in a 2D granular material under cyclic pure shear result from a structural anisotropy, coupling volumic and deviatoric component in the stress tensor.

In Fig. 2, we check the relevance of Eq. 3 for the two examples shown in Fig. 1. For this purpose, we introduce the peak amplitude of the pressure fluctuations,  $\Delta P = R\gamma_m^2/2$ , stemming from the quadratic dependency  $\gamma^2(t) = \gamma_m^2 \sin^2(\omega_0 t) = (\gamma_m^2/2)[1 - \cos(2\omega_0 t)]$ . At first, the Figs. 2a and 2b reveal that the spectral component of the normalized pressure fluctuation  $\delta P/\Delta P$  is mostly located at twice the driving frequency  $f_0$  prescribed by the quasi-harmonic shear strain  $\gamma/\gamma_m$ . Such a frequency conversion is typical of a quadratic dependency, consistently with the reliable quadratic fit shown in Figs. 2c and 2d. The estimated values of  $R$  from these fits,  $R = 4.49$  GPa for  $(\phi, P) = (0.64, 257$  MPa) and  $R = 7.54$  GPa for  $(\phi, P) = (0.70, 929$  MPa), indicate that  $R$  is a growing function of  $P$  and  $\phi$ . In more details, the Appendix Sec. A2 reveals a power law of the pressure,  $R \propto P^m$  with  $m \simeq 0.37$ , see Fig. A2b, consistently with the aforementioned power law of the packing fraction,  $R \propto (\phi - \phi_c)^n$  with  $n \simeq 0.56$ , see Fig. A2a.

Finally, we observe on Fig. 1c that the lower the packing fraction or the pressure, the greater  $\delta P/P$ . This observation is compatible with the evolution of the nonlinear behavior evidenced in Figs. 1d and 1e: the pressure being a state variable, its fluctuation with the shear deformation will likely make the mechanical response nonlinear. Indeed, the elasticity of granular media relies on Hertz contact theory, see above in Sec. 2, which depends on the confining pressure, see below in Sec. 4.1: a significant fluctuation of the pressure implies a nonlinearity of the elasticity. At first in the following, we will thus restrict our description to cases at sufficiently small  $\delta P/P$ , i.e. at large packing fractions and pressures, in order to deal with linear elasticity; next, we will account for additional nonlinear contributions at smaller packing fractions and pressures.

### 3.3 Elasto-hysteretic behavior

Here, we aim at reducing the complexity of the description of numerous particles submitted to shear, by identifying a low order approximation depending on essential parameters only. To reveal this model, we first focus on the example with weak relative fluctuation of  $P$ , at  $(\phi, \gamma_m) = (0.70, 0.15)$  from Fig. 1d. The stress-strain relation of this example is reproduced in Fig. 3.

At first glance, one sees that such a mechanical response is likely to be decomposed with a hysteretic response (a path-dependent saturating contribution) superimposed with a proportional response (a straight line with constant slope). In the following, we propose to describe the former with the Dahl model [51, 52], while the latter is expressed as a linear elastic term. Such an elasto-hysteretic decomposition was also used to describe the response of fibrous materials submitted to shear deformation [53]. The Dahl model is classically used in control engineering as an empirical model due to its implementation facility; in particular, it was shown to constitute an alternative formulation of the Mindlin frictional interaction between a sphere and a plane [54]. The shear stress is thus expressed as

$$\tau(\gamma) = \tau_D(\gamma, \dot{\gamma}) + G_E \gamma \quad (4)$$

where  $G_E$  corresponds to a linear shear modulus and  $\tau_D$  is the hysteretic Dahl stress. The latter has no explicit form, but it can be expressed in a compact form, as a first order time derivative nonlinear equation,

$$\dot{\tau}_D = G_D \dot{\gamma} \left[ 1 - \left( \frac{\tau_D}{\mu_D P} \right) \text{sign}(\dot{\gamma}) \right]^{n_D}, \quad (5)$$

where  $G_D$ , the first parameter of Dahl's model, is homogeneous to a shear modulus and corresponds to the slope of  $\tau_D(\gamma)$  when  $\tau_D = 0$ . The second parameter,  $\mu_D$ , corresponds to a Coulomb friction coefficient so that  $\mu_D P$  is the asymptotic value of  $\tau_D$  at large shear strain. The third parameter, the exponent  $n_D$ , controls the shape of the curve, e.g.  $n_D < 1$  exhibits brittle behaviors, while  $n_D > 1$  renders ductile responses. In the following of the study, we choose  $n_D = 1$  as a first attempt, in line with the literature [53, 55, 56], to model elasto-plastic behaviors in between ductile and fragile.

The parameter identification consists in finding the optimal parameters triplet  $(\mu_D^{\text{opt}}, G_D^{\text{opt}}, G_E^{\text{opt}})$  that minimizes the difference between the reduced model defined in Eqs. 4 and 5, and the steady mechanical response simulated with DEM. More details on the process of identification is given in the Appendix Sec. A3. To demonstrate the reliability of such identification, we show the root mean square error (RMSE) between  $\tau(\mu_D, G_D, G_E)$  and  $\tau_{\text{DEM}}$  across

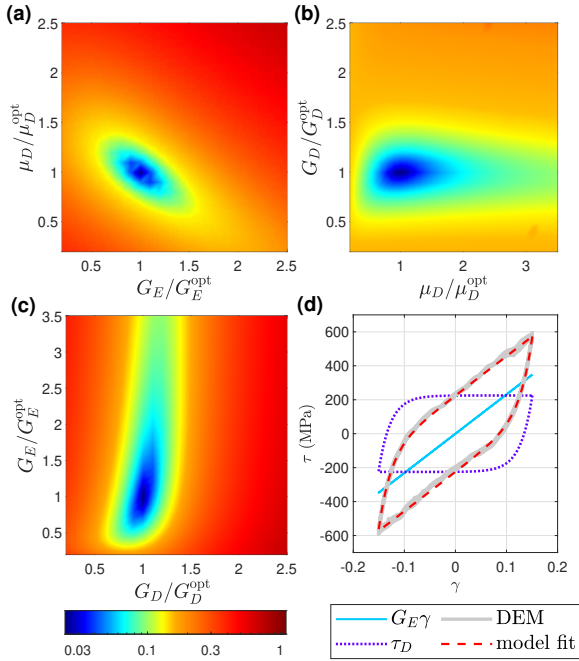


**Fig. 3** (a,b,c) Maps of the RMSE between  $\tau(\mu_D, G_D, G_E)$  and  $\tau_{\text{DEM}}$  plotted in the three planes  $(\mu_D, G_E)$ ,  $(\mu_D, G_D)$  and  $(G_D, G_E)$ , for the example  $(\phi, \gamma_m) = (0.70, 0.15)$  shown in Fig. 1d. The parameters are scaled by the optimal triplet  $\mu_D^{\text{opt}} = 0.24$ ,  $G_D^{\text{opt}} = 9.7$  GPa and  $G_E^{\text{opt}} = 2.3$  GPa. (d) Stress-strain relation from DEM simulation superimposed to the fits. The purple dotted line represent the hysteric Dahl contribution  $\tau_D(\gamma)$ , the solid blue line represents the linear contribution  $G_E\gamma$ , see Eq. 4, and the red dashed line is the sum of the two.

three cross-sections of the parameters space, see Figs. 3a, 3b, and 3c. One can see that an unique and well-defined global minimum exists in a wide region of parameters. The qualitative agreement of the fit is shown on Fig. 3d for the example  $(\phi, \gamma_m) = (0.70, 0.15)$ , and the quantitative agreement is illustrated in ore details in the Appendix Sec. A3 on Fig. A3.

### 3.4 Energy dissipation

The hysteresis of the macroscopic stress-strain relation evidenced in Fig. 3 renders the mechanical response non-conservative because of a path-dependent mechanical loading/unloading. Likely being the fingerprint of the microscopic inter-particle friction inside the granular sample, such a mechanism thus introduces energy dissipation; we aim in this subsection at defining and quantifying

the damping properties of our system. In the following, the dissipated energy per volume unit and per cycle is measured as

$$E_{\text{diss}}^{\text{cycle}} = \frac{1}{n} \oint_n \tau d\gamma, \quad (6)$$

which represents the enclosed area inside the hysteresis loop. This quantity has to be contrasted with the maximum stored energy reached during a cycle. The simplest estimation of that energy is [57]

$$E_{\text{stored}}^{\text{max}} \simeq \frac{1}{2} \tau_m \gamma_m. \quad (7)$$

The ratio between these two energies gives an estimation of the loss factor  $\eta$  as

$$\eta = \frac{E_{\text{diss}}^{\text{cycle}}}{2\pi E_{\text{stored}}^{\text{max}}}. \quad (8)$$

As an example, the definitions Eqs. 6-8 applied to the simulated strain-stress relation shown in Fig. 3d indicate that dissipated energy per cycle is  $E_{\text{diss}}^{\text{cycle}} \simeq 114$  J/cm<sup>3</sup>, whereas the maximum stored energy is  $E_{\text{stored}}^{\text{max}} \simeq 45$  J/cm<sup>3</sup>, leading to a loss factor  $\eta \simeq 0.40$ . Such a level of damping is worthy of interest in engineering applications. For sake of comparison, an efficient viscoelastic material such as *Deltane 350* from *Paulstra* manufacturer, a synthetic elastomer commonly used in the aeronautics field, ranges from lower value  $\eta \simeq 0.16$  at 1 Hz to a higher value  $\eta \simeq 0.88$  at 100 Hz, reaching  $\eta \simeq 0.45$  at 10 Hz [28, p.94]. In contrast with the frequency-independent friction-based dissipation observed in our granular medium, the polymer material thus loses its efficiency at low frequency, in addition to being strongly temperature dependent [28, p.76].

### 3.5 Parametric study

We now look at generalizing our observations for various configurations in the parameter space. In particular, we seek at elucidating the possibility of an *optimal regime* for energy dissipation, in between low confinement pressure (where the particles freely flow on top of each other without rubbing) and high confinement pressure (where the particles firmly stick to form a sturdy elastic brick). Three families of parameters are distinguished, namely (i) the particle properties, (ii) the state variables defining the packing and (iii) the

external parameters defining the driving excitation.

The *particle properties* include their Young modulus  $E_p$ , Poisson ratio  $\nu_p$ , mass density  $\rho_p$ , radius  $r_p$ , number  $N_p$  and the inter-particle friction coefficient  $\mu_p$ . For sake of simplicity, fictional materials are considered, for which those parameters are varied independently; however, they range within realistic values, as for the Young modulus  $E_p$  reported in Tab. 1. Without loss of generality, we assume that the Poisson ratio has a negligible effect (it only contributes to a second order correction of the elasticity, see Eqs. 1 and 2) so that it is arbitrarily kept constant in this study, equal to its nominal value  $\nu_p = 0.27$ . Also, the mechanical response should be independent of the mass of the particles at sufficiently low driving frequency (see below, in the quasi-static regime), the mass density considered in the following parametric study has a nominal value  $\rho_p = 7850 \text{ kg/m}^3$ . In the same manner, it is likely that the size and the number of particles should not play a role at the macroscopic scale, in the long wavelength (low frequency, see below) continuum limit approximation. The insensitivity of the mass, the size and the number of the particles is probed at once successfully by simulating a sample made of particles with half the average radius (i.e. one eighth of the mass per particle) but same sample's volume (i.e. eight times more particles) without noticeable difference compared to the nominal case; this case is shown in the Sec. 4.1. Finally, the effect of inter-particle friction coefficient  $\mu_p$  is probed separately, over more than a decade, in Sec. 4.2.

The *state variables* include the packing fraction  $\phi$ , the pressure  $P$  and the coordination number  $Z$ , see Tab. 1. These three quantities are related: according to the literature [48], we checked (result not shown, see [49, p.111]) that  $P \propto (\phi - \phi_c)^{3/2}$  and  $(Z - Z_c) \propto (\phi - \phi_c)^{1/2}$  where  $\phi_c = 0.595 \pm 0.003$  (0.5%) and  $Z_c = 5.042 \pm 0.085$  (1.7%) are values of the packing fraction and coordination number at the critical point where the jamming occurs. Thus, imposing the packing fraction  $\phi$  sets the average level of pressure  $P$  and the average contact number  $Z$ .

Finally, the *external parameters* include the excitation angular frequency  $\omega_0 = 2\pi f_0$  and shear amplitude  $\gamma_m$ , see Tab. 1. The former is kept low enough, to fulfill a quasi-static regime where the

**Table 1** Parameter space.

Parameter	value	unit
$E_p$	3 ~ 300	GPa
$\nu_p$	0.27	-
$\rho_p$	7850	kg/m <sup>3</sup>
$r_p$	(0.5 ~ 1.0) $\pm$ 25%	mm
$N_p$	1000 ~ 8000	-
$\mu_p$	0.017 ~ 0.6	-
$\phi$	0.60 ~ 0.71	-
$P$	15 ~ 1300	MPa
$Z$	5.69 ~ 7.91	-
$\omega_0$	quasi-static	rad/s
$\gamma_m$	0.005 ~ 0.15	-

inertia of the grains does not produce any contribution in the force balance. The latter is kept constant, in the parametric study presented in Secs. 4.1 and 4.2, at a nominal value  $\gamma_m = 0.15$  that ensures observing noticeable hysteresis in the stress-strain relation, as in Figs. 1d and 1e for instance. The dataset is then completed by probing different amplitudes, in Secs. 4.3 and 4.4.

For each configuration of the parameters space, the system is simulated using DEM, from which we estimate the stress-strain curve in shear as described in Sec. 2. Then, an optimal triplet of parameters ( $\mu_D, G_D, G_E$ ) relying on the elasto-hysteretic reduced model are retrieved according to the protocol described in Sec. 3.3. These three parameters are plotted versus the state variable  $P$  in Fig. 4a and 4b for a wide range of particle properties. For dimensional reasons, we normalize the pressure  $P$  and the elasticity  $G_{E,D}$  by the inter-particle contact stiffness (proportional to the Young's modulus of the particles material) in the normal direction,  $k_n \propto E_p$ , as defined in Eq. 1. One can see on Fig. 4a that both  $G_E$  and  $G_D$  increase with  $P$ , over a decade, resulting in two clearly defined but distinct slopes which will be analyzed in-depth in the Sec. 4. In contrast, the effective Coulomb friction coefficient  $\mu_D$  shown in Fig. 4b appears weakly dependent of the confinement pressure and of the particle properties, with an average value  $\langle \mu_D \rangle \simeq 0.28$ .

Finally, we look at the energetical performances of the granular packing, as defined in Eqs. 6-8; again, we normalize the energies per unit volume by  $k_n$  (i.e. by the particle's Young Modulus) for dimensional reasons. One sees on Fig. 4c that both the dissipated and the maximum stored energy per cycle increase as functions of the



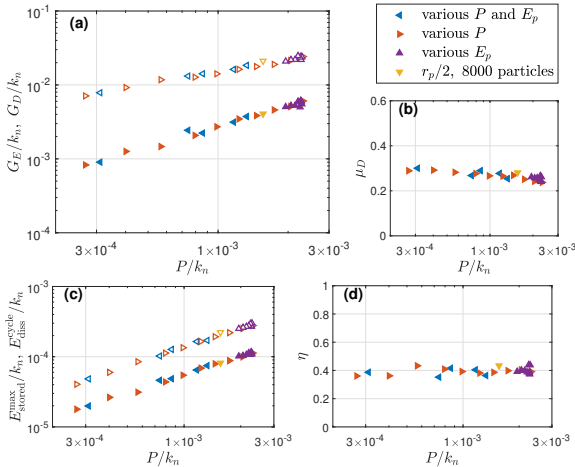


**Fig. 4** (a): Dimensionless fitted parameters  $G_D/k_n$  (open symbols) and  $G_E/k_n$  (solid symbols) for various volume fraction  $\phi$  and elasticity  $E_p$  as functions of the dimensionless pressure  $P/k_n$  at  $\gamma_m = 0.15$ . (b): Dahl friction coefficient against dimensionless pressure for the same data set. (c): Dissipated energy per cycle (open symbols) and maximum stored energy (solid symbols) computed from hysteresis response using Eqs. 6 and 7 respectively, as functions of the dimensionless pressure. (d): Loss factor computed from 8, as function of the dimensionless pressure. Legend symbols are common for (a-d).

confinement pressure, consistently with the elastic features of the effective model,  $G_E$  and  $G_D$ . Also in agreement with the effective Coulomb friction coefficient  $\mu_D$ , their ratio (i.e. the loss factor), shown in Fig. 4d, appears weakly dependent of the pressure and the particle properties, lying close to the value  $\eta = 0.40$  already observed in Fig. 3d.

## 4 Discussion

### 4.1 Effective elasticity

It is observed in Fig. 4a that the identified elastic moduli  $G_D$  and  $G_E$  are both correlated to the confinement pressure  $P$ . Such a behavior is expected in granular material. Indeed, focusing on the low amplitude regimes, such that  $\tau_D \ll \mu_D P$ , the asymptote of the reduced model defined in Eq. 4 and 5 indicates that  $\tau \rightarrow (G_E + G_D)\gamma$ . Hence, a total shear modulus of the granular packing,

$$G_T = G_E + G_D, \quad (9)$$

appears relevant to describe the elastic response of the layer of particles in the infinitesimal limit. It turns out that  $G_T$  corresponds to the effective

shear modulus defined by Walton's [13] effective medium theory (EMT) of granular materials. This theory is based on Hertz contact mechanics [14, 15] under a mean field approximation (long wavelength continuum limit) of small perturbations and uniform strain (i.e. affine deformations [46]). For purely frictionless particles (tangential slip,  $\mu_p = 0$ ), the EMT's effective bulk and shear moduli are

$$K_{\text{EMT}}(P) = \frac{k_n}{12\pi} (\phi Z)^{\frac{2}{3}} \left( \frac{6\pi P}{k_n} \right)^{\frac{1}{3}}, \quad (10)$$

$$G_{\text{EMT}}^0(P) = \frac{k_n}{20\pi} (\phi Z)^{\frac{2}{3}} \left( \frac{6\pi P}{k_n} \right)^{\frac{1}{3}}, \quad (11)$$

respectively, where the contact stiffness  $k_n$  between particles in the normal direction is defined in Eq. 1,  $Z$  is the coordination number, and  $P$  is the mean (time average) hydrostatic pressure defined in Eq. 3. For infinitely frictional particles (i.e. tangential stick,  $\mu_p \rightarrow \infty$ ), the effective bulk modulus remains unchanged but the effective shear modulus,

$$G_{\text{EMT}}^\infty(P) = \frac{k_n + (3/2)k_t}{20\pi} (\phi Z)^{\frac{2}{3}} \left( \frac{6\pi P}{k_n} \right)^{\frac{1}{3}}, \quad (12)$$

is enhanced due to the contribution of the inter-particles contact stiffness in the tangential direction,  $k_t$ , defined in Eq. 2. The expressions Eqs. 10-12 indicates the typical scaling  $G_{\text{EMT}}^{0,\infty} \propto K_{\text{EMT}} \propto E_p(P/E_p)^{1/3}$  inherited Hertzian contact interaction. Finally, it is worth reminding that the volume fraction and the coordination number are also pressure dependent [48],  $\phi(P)$  and  $Z(P)$ , as pointed out in Sec. 3.5.

The plot in Fig. 5a of the total shear modulus versus the frictional effective modulus given in Eq. 12 reveals a close correlation

$$G_T = \alpha G_{\text{EMT}}^\infty \quad (13)$$

with a well-defined coefficient of proportionality,  $\alpha = 0.687 \pm 0.073$  (10.6%), in average over a dataset which is restricted to an inter-particles friction coefficient  $\mu_p = 0.15$ . In line with the EMT model, the value of the prefactor relies on the inter-particle friction coefficient: the formula given by Eqs. 11-12 indicate two asymptotic values  $\alpha = G_{\text{EMT}}^0/G_{\text{EMT}}^\infty = 1/(1 + 3k_t/2k_n) \simeq 0.4$  for

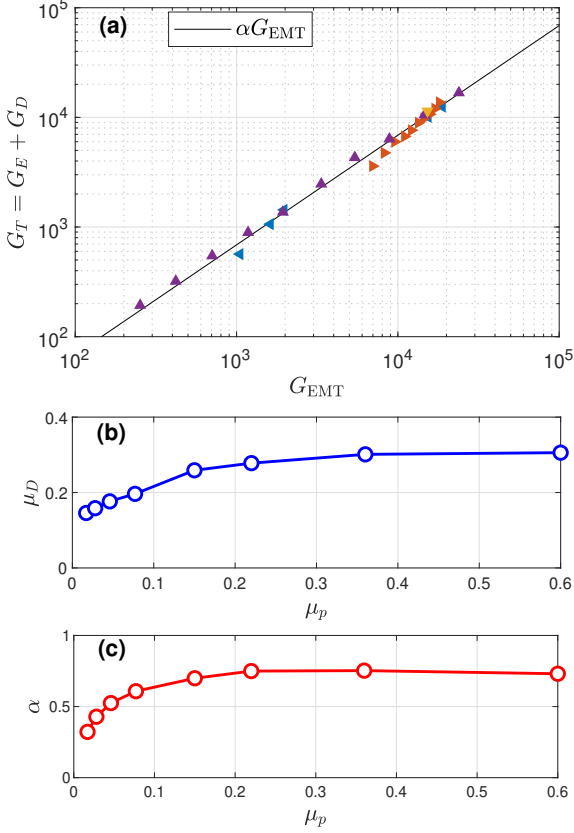


**Fig. 5** (a): Total shear modulus  $G_T = G_D + G_E$  versus effective shear modulus  $G_{EMT}^{\infty}$  (Eq. 12) with a linear fit of slope  $\alpha = 0.687 \pm 0.073$  (10.6%). Same legend as in Fig. 4. (b,c): identified Dahl friction coefficient  $\mu_D$  and coefficient  $\alpha$  as functions of the inter-particles friction  $\mu_p$ .

frictionless particles and  $\alpha = G_{EMT}^{\infty}/G_{EMT}^{\infty} = 1$  for frictional ones. The value of  $\alpha$  at an intermediate  $\mu_p = 0.15$  is thus consistent with these bounds.

## 4.2 Effective friction

We defined in Eq. 5 and reported in Fig. 4b a friction coefficient according to a Dahl model, as the ratio between the asymptotic stress at large strain and the confinement pressure. In the field of the rheology of granular flow [16], a similar definition of an effective friction coefficient exists as the ratio of shear to normal force at the wall, or as the ratio of the shear stress to the pressure inside the material,

$$\mu(I) = \tau/P, \quad (14)$$

which is known to depend on a single dimensionless inertial number [20, 21],  $I = t_p/t_s$ . The number  $I$  is the ratio between two time scales, namely, the typical time  $t_s = 1/\dot{\gamma}$  associated to shear rate, which correspond to the macroscopic deformation duration, and  $t_p = r_p/\sqrt{P/\rho_p}$  the one related to confinement, corresponding to the typical duration of microscopic rearrangement during which a grain moves by one neighbor size due the confining pressure [18]. The ratio  $I$  describes the regime of a granular flow, from the quasi-static limit at low  $I$  to the kinetic regime with multiple collisions at high  $I$ . A phenomenological equation [21] provides an estimation of the effective friction coefficient,

$$\mu(I) = \mu_s + \frac{\mu_g - \mu_s}{I_0/I + 1}, \quad (15)$$

where  $I_0$  is a constant of the order of unity, which delimits the two asymptotic limits. The effective friction coefficient value  $\mu_g$  accounts for the existence of a gaseous phase at high inertia [18],  $I \gg I_0$ . In turn, the quasi-static value of the effective friction coefficient,  $\mu_s$ , mostly depends on the inter-particle friction coefficient  $\mu_p$  [58]. In practice, the estimated inertial number probed in our study remains small,  $10^{-5} \leq I \leq 10^{-4}$ , thanks to the low driving frequency (see Sec. 2), in such a way that the effective friction does not depend on the inertial number but only on the inter-particle friction coefficient,  $\mu(I \ll I_0) \simeq \mu_s(\mu_p)$ . Consistently, the analysis of the dependence of the Dahl's effective friction coefficient,  $\mu_D$ , as a function of the inter-particle one,  $\mu_p$ , is shown on Fig. 5b, all other parameters being fixed. In particular, we observe that  $\mu_D$  is an increasing function of  $\mu_p$  with a saturation, in qualitative and quantitative agreements with the literature, see for instance Ref. [58].

Finally, we check the dependence of the prefactor  $\alpha$  defined in Eq. 13 with respect to  $\mu_p$ . As expected in Sec. 4.1,  $\alpha$  should be a function of  $\mu_p$ , accounting for the transition between perfectly frictionless,  $\alpha \simeq 0.4$ , and infinitely frictional particles,  $\alpha = 1$ . The observation reported in Fig. 5c is in qualitative agreement with this expectation, showing that the prefactor  $\alpha$  increases with the inter-particle friction coefficient  $\mu_p$  until saturating to a value of the order of unity.

### 4.3 Dimensional analysis

We determined in Sec. 3.5 that the mechanical response depends on numerous particles features ( $E_p$ ,  $\nu_p$ ,  $\rho_p$ ,  $r_p$ ,  $N_p$  and  $\mu_p$ ), state variables ( $P$ ,  $Z$ ,  $\phi$ ) and external parameters ( $\omega_0$  and  $\gamma_m$ ). However, Sec. 4.1 and 4.2 show that most of these parameters are linked with each other. Here, we aim at reducing the dimension of the parameters space, by making use of the observations presented in Sec. 3.3. In particular, we use the fact that the stress strain response is well described by an elasto-hysteretic model given by Eq. 4 and 5. We thus choose to rewrite these equations in dimensionless form using the following quantities:

$$\Gamma = \frac{\gamma}{\gamma_m}, \quad \mathbb{T} = \frac{\tau}{G_T \gamma_m},$$

$$\xi = \frac{\mu_D P}{G_T \gamma_m} \quad \text{and} \quad \Psi = \frac{G_E}{G_T} = 1 - \frac{G_D}{G_T}, \quad (16)$$

with  $\Gamma$  and  $\mathbb{T}$  the dimensionless shear strain and stress, respectively normalized by the amplitude of the shear strain and a typical shear stress proportional to the total shear modulus  $G_T$  defined in Eq. 9. In line with this choice, it stands to reason that the Dahl's effective friction coefficient  $\mu_D$  can be represented by a non-dimensional parameter  $\xi$ , the *first parameter* of our model, resulting from the competition between the typical shear stress imposed to the granular medium,  $G_T \gamma_m$ , and a Mohr-Coulomb-like threshold  $\mu_D P$ . According to Fig. 4, the parameter  $\xi$  is essentially a function of  $P/k_n$  and  $\gamma_m$ . In turn, the elastic term added to the hysteretic contribution, see Eqs. 4 and 5, can be described by a second parameter,  $\Psi$ , which stands as a *partition parameter* quantifying the ratio between the purely elastic shear modulus,  $G_E$ , and the one stemming from the hysteretic response,  $G_D$ . According to the normalizations defined in Eq. 16, the model Eqs. 4 and 5 rewrites

$$\dot{\mathbb{T}} = \dot{\Gamma} \left[ 1 - \left( \frac{1 - \Psi}{\xi} \right) (\mathbb{T} - \Psi \Gamma) \text{sign}(\dot{\Gamma}) \right], \quad (17)$$

revealing that the mechanical response  $\mathbb{T}(\Gamma)$  only depends on two parameters,  $\xi$  and  $\Psi$ . From a physical point of view, the parameter  $\xi$  provides an information on the degree of hysteresis (related to frictional stress,  $\mu_D P$ ) and elasticity (related to elastic stress,  $G_T \gamma_m$ ) of the response, suggesting that  $\Psi$  should be also a function of  $\xi$ .

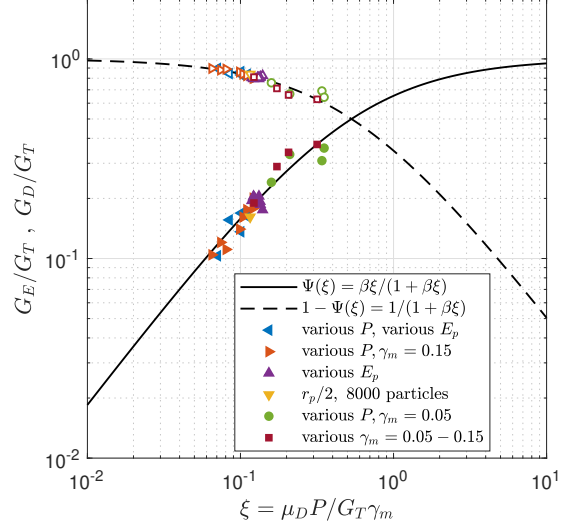


**Fig. 6** Partition parameter  $\Psi(\xi)$  as defined in Eq. 16, as a function of the dimensionless parameter  $\xi = \mu_D P / G_T \gamma_m$ . The solid line is the Ansatz introduced in Eq. 18 with  $\beta = 1.882 \pm 0.254$  (13.5%) best fitting the dataset.

Such an expectation is checked in Fig. 6, which reveals a correlation between  $\Psi$  and  $\xi$ . In practice, the dependency is probed in the small-to-moderate values of  $\xi$  only (see Fig. 1d for instance), where an hysteresis is clearly observable and leads to accurate estimations of the triplet  $(\mu_D, G_D, G_E)$  i.e. of a pair  $(\Psi, \xi)$ . For larger  $\xi$  (i.e. high pressure  $P$  or low amplitude  $\gamma_m$ ), the mechanical response tends to an elastic one, which prevents distinguishing the elasto-hysteretic contributions and leads to poorly accurate estimations of  $\Psi$  and  $\xi$ . However, considering that the granular medium becomes purely elastic in the high  $\xi$  regime provides the information that the partition parameter  $\Psi$  saturates to 1. Hence, the simplest saturating function takes the form

$$\Psi(\xi) = \frac{\beta \xi}{1 + \beta \xi}, \quad (18)$$

where  $\beta$  is an adjusting parameter. Fitting the Ansatz given in Eq. 18 to both  $G_E$  and  $G_D$  indicates that  $\beta = 1.882 \pm 0.254$  (13.5%). As intuited, the relation Eq. 18 thus shows that the model described by Eq. 17 only depends in fact on the unique parameter  $\xi$ . Note that for sake of completeness, the dataset shown in Fig. 6 is supplemented by simulations at various amplitudes,

$0.05 \leq \gamma_m \leq 0.15$ , in contrast with Fig. 4 where all simulations are done at  $\gamma_m = 0.15$  only.

#### 4.4 Loss factor

Here, we provide details about energy dissipation, in line with Sec. 3.4, at the light of the dimensional analysis provided in Sec. 4.3. In particular, we aim at probing how the dissipated energy Eq. 6, the stored energy Eq. 7 and the loss factor Eq. 8 depend on the non-dimensional parameter  $\xi$ . For this purpose, we compare in Fig. 7 the data simulated by DEM to the features of the reduced model. The mechanical response of the model,  $T(\Gamma)$ , is determined via explicit numerical time integration of Eqs. 17-18 for every  $\xi$ ; then one extracts the energetic features according to Eqs. 6-8. Note that for dimensional purpose, energies will be represented with respect to a reference energy,

$$E_{\text{ref}} = \frac{1}{2} G_T \gamma_m^2, \quad (19)$$

which stands for the energy stored by a purely elastic medium,  $\tau = G_T \gamma$ .

As expected from the analysis of Sec. 4.3, we observe on Fig. 7 that both energies and the loss factor are well correlated to  $\xi$ . The agreement between the data simulated by DEM and the reduced model is both qualitative and quantitative in the moderate range of  $\xi$ . From low-to-moderate  $\xi$ , the non-dimensional dissipated energy rises because increasing the pressure, for instance, raises the frictional dissipative force  $\mu_D P$ ; concurrently, the medium transits from a loose (at low Coulomb threshold) to a dense (at high Coulomb threshold) state, thus progressively gaining elasticity and the ability to store energy. In contrast at higher pressure, the particles firmly stick with each other and the sample tends to store energy as a purely elastic medium: from moderate-to-high  $\xi$ , the dissipated energy vanishes while the non-dimensional stored energy tends to unity. Consistently with these trends, the loss factor  $\eta$  appears relatively constant in the moderate range of  $\xi$  (see the colored markers in Fig. 7c,  $0.06 \leq \xi \leq 0.4$ ), in agreement with the observation in Fig. 4d that  $\eta$  appears fairly independent of the pressure within the same range of parameters. The trends also reveal a decrease of  $\eta$  which is characteristic of an elastic medium at high  $\xi$ ,

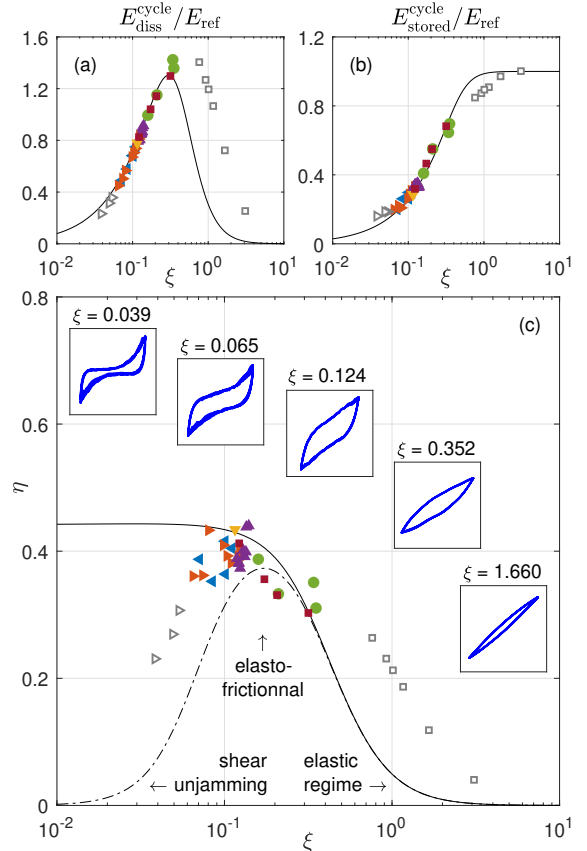


**Fig. 7** (a) Dissipated energy per cycle per volume unit, see Eq. 6, as a function of  $\xi$ , normalized to the reference energy defined in Eq. 19. (b) normalized stored energy per cycle per volume unit, see Eq. 7, versus  $\xi$ . (c) Loss factor  $\eta$  versus  $\xi$ , see Eq. 8. The legend of the colored markers is the same as in Fig. 6. Grey hollow symbols are supplementary points from DEM calculations at various small  $\gamma_m$  (hollow squares) and various low pressures (hollow triangles). The solid line is the reduced model Eq. 4, while the dashed line stands for the improved reduced model Eq. 21.

but in a range that is not accessed by the simulations. However, the reduced model reveals a plateau at low  $\xi$ , but again not evidenced by the DEM simulations.

On the *one hand*, we supplement six data at high  $\xi$  (white squares in Fig. 7) which tend to confirm the decay predicted by the model, namely, a jammed granular medium under high pressure behaves as an elastic solid (weak dissipation, high stored energy and thus low loss factor). On the *other hand*, the trend of the three data added at small  $\xi$  (white triangles in Fig. 7) reveals a decay of  $\eta$  which clearly differs from the prediction given by the reduced model. Interestingly, such a decay

is concomitant with the nonlinear stiffening inflection observed near the cusp points in Fig. 1e, at low  $P$  and high  $\gamma_m$ , concurrently with the significant relative fluctuation of the pressure shown in Fig. 1c. The buildup of such additional nonlinearity in the stress-strain response at low  $\xi$  is clearly evidenced in the examples  $\xi = 0.124$  to  $\xi = 0.039$  given in the inset of Fig. 7c.

#### 4.5 Weakly nonlinear response

As expected in the conclusions of Sec. 3.2 and from the developments of Sec. 4.1, the fluctuation of the pressure due to the frustrated dilatancy described in Eq. 3 is a potential source of nonlinearity of the elasticity, and thus an opportunity to improve the reduced model defined in Eqs. 4 and 5. In a first qualitative attempt, aiming at capturing such a nonlinearity in the stress-strain relation, we will only consider a correction in the effective elasticity defined in Eqs. 10-12, by arbitrarily leaving unchanged the pressure in the Coulomb stress,  $\mu_D P = \text{const}$  see Eq. 5. The first order Taylor expansion of the shear modulus defined in Eq. 13 provides

$$\begin{aligned} G_T(\tilde{P}) &= G_T(P) \times (1 + \delta P/P)^{1/3}, \\ &\simeq G_T(P) \times (1 + \rho \Gamma^2), \\ \rho &= R\gamma_m^2/3P = 2\Delta P/3P. \end{aligned} \quad (20)$$

The parameter  $\rho$  is proportional to the relative pressure fluctuation and quantifies the nonlinearity of the response, see the comments of Fig. 1e. At the lowest order, the expansion Eq. 20 thus leads to a nonlinear cubic correction term in the reduced model Eq. 4,

$$\begin{aligned} \tau(\gamma) &\simeq \tau_D(\gamma, \dot{\gamma}) + G_E \gamma + G_{NL} \gamma^3, \\ G_{NL} &= \rho G_T / \gamma_m^2 = R G_T / 3P. \end{aligned} \quad (21)$$

It is worth mentioning that this additional term is conservative, such that it only enhances the stored energy and does not affect the dissipated energy; it thus likely lowers the loss factor predicted by the reduced model, as observed in Fig. 7c at low  $\xi$  (low pressures  $P$  or high amplitudes  $\gamma_m$ ).

As an example, we examine the contribution of such a correction for the case  $(\phi, \gamma_m) = (0.64, 0.15)$  shown in Fig. 1e, for which  $\xi = 0.080$

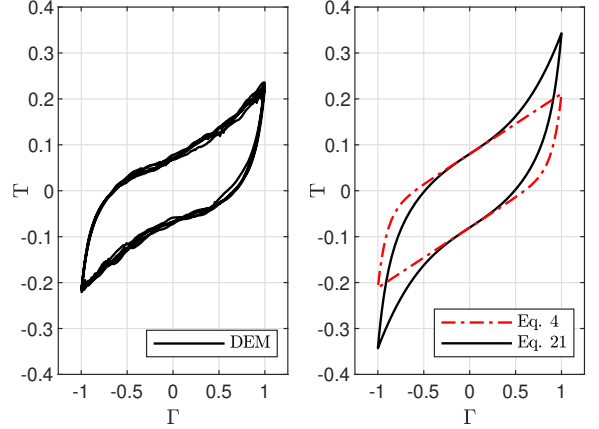


**Fig. 8** (a) Non-dimensional stress-strain curve of DEM simulation in the weakly nonlinear regime ( $\phi = 0.64$  at  $\gamma_m = 0.15$ , such that  $\xi = 0.080$  and  $\rho = 2\Delta P/3P \simeq 0.131$ ): the DEM simulated loss factor is  $\eta = 0.368$ . (b) Prediction given by the reduced model Eq. 4 (red dashed-dotted line, loss factor  $\eta = 0.438$ ) and by the improved reduced model Eq. 21 (black solid line, loss factor  $\eta = 0.270$ ). Compared to the DEM simulation, the former does not show the characteristic inflection near the cusp points, underestimates the peak amplitude of the stress by 11% and overestimates the loss factor by 19%; the latter qualitatively shows such an inflection, but overestimates the peak amplitude of the stress by 45% and underestimates the loss factor by 27%.

and  $\rho = 2\Delta P/3P \simeq 0.131$ , and whose DEM simulation is reproduced in Fig. 8a. As seen in Fig. 8b, the stress-strain relation predicted by the model defined in Eq. 4, see the red dashed-dotted curve, suffers from a poor agreement: the identification of the parameters described in Sec. 3.3 inherently matches the dissipated energy (see the area within the curve) and well catches an overall elasticity, but fails to reflect neither the slope at small strains (near  $\Gamma = 0$ ) nor the characteristic inflections at large strains (near  $\Gamma = 1$ ). The Eq. 21 provides a more convincing qualitative agreement, with  $G_{NL} = \rho G_T / \gamma_m^2$  estimated by using the value of  $G_T$  fitted by Eq. 4 and the value  $\rho = 0.131$  estimated from the pressure fluctuation, see the solid black line in Fig. 8b. However, the quantitative agreement is less obvious: the original model Eq. 4 overestimates the loss factor simulated by DEM by 19% whereas the improved model Eq. 21 underestimates it by 27%.

A better quantitative agreement can be reached by adjusting the parameters of Eq. 21 independently, since for instance the value of  $G_T$  obtained with Eq. 4 is poorly relevant in the weakly nonlinear regime. However,

the identification of a set of four parameters,  $(\mu_D, G_D, G_E, G_{NL})$ , introduces numerical uncertainties that require a protocol as careful as the one detailed in Fig. 3. An even more reliable improvement is to consider also the pressure fluctuation not only on the elastic contribution, as in Eq. 21, but in the hysteretic part too. However, both these additional improvements are beyond the scope of our qualitative attempt.

Nevertheless, the dimensional analysis of Eq. 21, derived as in Sec. 4.3, straightforwardly shows that it depends on the two non-dimensional parameters  $\xi$  and  $\rho$  only. Attempting to reduce further the description of the model, we consider that  $\xi$  is essentially a function of  $P/k_n$  and  $\gamma_m$  and we probe the correlations of  $\rho$  with the same two parameters, as detailed in Figs. A2c and A2d of the Appendix Sec. A2. Understanding such dependencies is out of the scope of the present paper. However, they allow estimating an improved version of the loss factor in a smaller parameter space,  $\eta(\xi(P/k_n, \gamma_m), \rho(P/k_n, \gamma_m))$ . This improvement is exemplified in Fig. 7c (dashed-dotted black curve) for the nominal case  $\gamma_m = 0.15$  and the pressure dependent  $\rho$  as defined on Fig. A2c. The plot shows a trend of the loss factor at low  $\xi$  that qualitatively agrees with DEM simulations (see the hollow triangles calculated at low pressures), thus demonstrating that the lowering of  $\eta$  likely results from the nonlinearity of the elasticity near the unjamming condition.

From the practical point of view, the decay of the loss factor  $\eta$  at both low and high  $\xi$  leaves a decade wide region, around  $0.05 < \xi < 0.5$ , where the loss factor is maximal and ranges in between 20% and 40%. Technically, this provides an opportunity to tune the dissipation in order to target specific operating points, by adjusting for instance the confinement pressure to mitigate efficiently a given range of vibrations amplitudes. Interestingly, the optimal value  $\eta \simeq 40\%$  is independent of the particle properties.

## 5 Conclusion

In this paper, an elasto-hysteretic model describing a simply sheared granular medium confined in a box with rigid but moving walls has been studied using discrete element method. In particular, it was shown that a single degree-of-freedom

Dahl model coupled with an elastic response reliably describes the behavior simulated by DEM, in terms of the stress-strain relation, the stored and the dissipated energies, and the loss factor. The well-known effective medium theory predicting the elasticity of granular media, and a macroscopic effective friction coefficient, were identified as the main parameters of this model, via an extensive parametric study derived as a function of the confining pressure and the features of the particles and the mechanical excitation.

Our study reveals that the elasto-hysteretic mechanical response of the granular medium mainly depends on a single dimensionless parameter, namely  $\xi$ , akin to a normalized Coulomb threshold. This parameter allows quantifying *a priori* how hysteretic versus how elastic is the mechanical response of our apparatus. The regime at high value of  $\xi$  (i.e. high confinement pressure or low shear amplitudes) is asymptotically elastic, such that the loss factor vanishes in this regime. Nevertheless, the proposed model fails at low value of  $\xi$  (i.e. low pressure or high shear amplitudes) due to large pressure fluctuation resulting from the anisotropy of the contact network. This effect leads to an additional nonlinearity of the elasticity, which ultimately results in the decrease of the damping ratio in this regime. Hence, in an intermediate range of  $\xi$ , the dissipation is dominated by an effective friction coefficient that is mostly independent of the particles features, whereas the stored energy is dominated by an effective elasticity that mostly depends on the confinement pressure and the elasticity of the particle. It thus results that the loss factor can be tuned by the confinement pressure, its maximum being independent of the particles and of the operating point.

From the practical point of view, the reduced model derived in this study can be used in a more complex configurations, such as a granular medium clamped in between elastically bending beams to form a composite structure aiming at dissipating mechanical vibrations. Here, the advantage of a reduced model is to lower the complexity and the numerical cost of simulations coupling discrete element method with finite element method, hence allowing subsequent optimization process, for instance. The attempt to design a granular composite beam is a perspective

under our consideration [49]. Also, the seminal features of this study has been patented [44] by some of us in a separate work conducted in collaboration with *Safran Spacecraft Propulsion*, a major stakeholder of the Aeronautic Industry. The patented equipment aims at mitigating the vibrations of a cathode in the harsh environment of a spacecraft plasma engine, by using non-cohesive ceramic particles confined inside structural elements, as described in the present study.

## Appendix

### A1 Particle deformation

Provided that the contact between particles follows Hertz theory, the average contact strain in a jammed granular packing can be calculated according to Roux *et al.* [50]

$$\langle (h/a)^{2/3} \rangle^{3/2} = \left( \frac{3\pi}{Z\phi} \right)^{2/3} \left( \frac{P}{k_n/2} \right)^{2/3}, \quad (\text{A1})$$

where  $h$  corresponds to the contact overlap and  $a$  to the particle diameter. In our study, the average contact strain ranges between 0.5% and 4%, see Fig. A1.

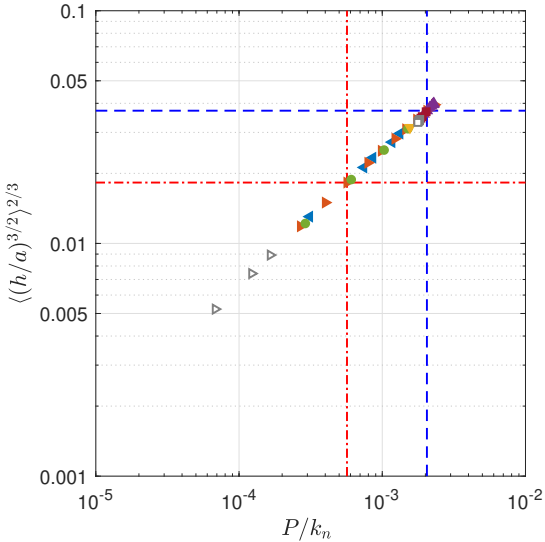


**Fig. A1** Average contact strain as a function of the dimensionless pressure. Dashed-dotted red line and dashed blue line correspond to the computations from Figs. 1d and 1e at  $(\phi, \gamma_m) = (0.64, 0.15)$  and  $(\phi, \gamma_m) = (0.70, 0.15)$ , respectively. Legend of the symbols is the same as in Fig. 6.

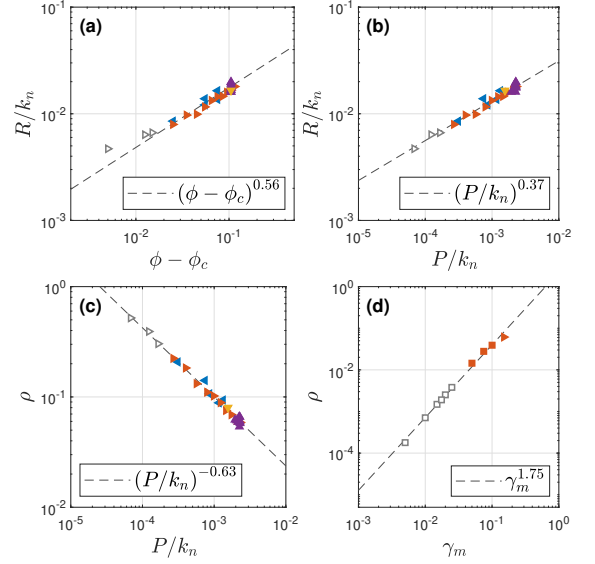


**Fig. A2** (a-b) Scaling of the normalized Reynolds coefficient  $R$  with respect to the packing fraction and (b) to the dimensionless confining pressure, both at constant  $\gamma_m = 0.15$ . (c-d) Scaling of the nonlinear parameter  $\rho = 2\Delta P/3P$  with respect (c) to the dimensionless pressure at constant  $\gamma_m = 0.15$  and (d) to the shear strain amplitude at constant  $k_n$  and  $P$ . Equations of the fits in dashed lines are  $R/k_n = 0.06(\phi - \phi_c)^{0.56}$ ,  $R/k_n = 0.18(P/k_n)^{0.37}$ ,  $\rho = 1.33 \times 10^{-3}(P/k_n)^{-0.63}$  and  $\rho = 2.22\gamma_m^{1.75}$ , respectively.

### A2 Nonlinear parameter

The effect of the nonlinearity resulting from the pressure fluctuation at low  $\xi$  can be quantified by looking at the dependence of the Reynolds coefficient  $R$  defined in Eq. 3 with the state variables  $P$  or  $\phi$  (both are related), and at the dependence of the nonlinear parameter  $\rho = 2\Delta P/3P$  defined in Eq. 20 with the pressure  $P$  and the amplitude  $\gamma_m$ . Results are displayed on Fig. A2, showing well defined tendencies : (i)  $R$  is an increasing function of a power law of the relative packing fraction  $(\phi - \phi_c)$ ; (ii) coherently,  $R$  is an increasing function of a power law of the confining pressure  $P$ ; (iii)  $\rho$  is a decreasing function of  $P$ , meaning that loose packing leads to strong nonlinearity at a given amplitude  $\gamma_m$ ; (iv)  $\rho$  is an increasing function of  $\gamma_m$ , meaning that nonlinearity classically increases with the amplitude of perturbation.

### A3 Parameter fitting procedure

The fitting of the parameters  $(\mu_D, G_D, G_E)$  described in Secs. 3.3 and 3.5 is realized in

two steps: the determination of an initial guess  $(\mu_D^{\text{ini}}, G_D^{\text{ini}}, G_E^{\text{ini}})$  by successive steps, followed by one refinement to obtain an optimal triplet  $(\mu_D^{\text{opt}}, G_D^{\text{opt}}, G_E^{\text{opt}})$ . We first look for an initial ensemble  $G_D^{\text{ini}}(\mu_D)$ , as a function of a finite number of friction coefficient taken in a finite interval  $0.01 \leq \mu_D \leq 10$ , which provides a hysteresis loop given by the model Eq. 4 having the same dissipated energy as in the DEM simulation. This step is made possible because, among the three parameters to fit, the dissipated energy does not depend on the conservative contribution associated with  $G_E$ . In practice, we determine  $G_D^{\text{ini}}$  at a given  $\mu_D$  by minimizing (using *Matlab's* simplex algorithm *fminsearch*) the root-mean-square error (RMSE) between the area within one stress-strain close loop estimated (using *Matlab's* numerical integration *trapz*) by the model Eq. 4 and by the DEM simulation. This step provides a discrete numerical function,  $G_D^{\text{ini}}(\mu_D)$ , with which we then search for a value  $G_E^{\text{ini}}(\mu_D)$  that minimizes the RMSE between the instantaneous stress response given by the model Eq. 4 and that of the simulation, at any given  $\mu_D$ . Finally, the initial guess  $\mu_D^{\text{ini}}$

is the value that provides the lowest aforementioned RMSE. The triplet  $(\mu_D^{\text{ini}}, G_D^{\text{ini}}, G_E^{\text{ini}})$  thus constitutes a reliable starting point to perform a 3-parameters minimization of the RMSE between the model Eq. 4 and the simulated instantaneous stress response, defined by the following cost function :

$$C(\mu_D, G_D, G_E) = \frac{\sqrt{\langle [\tau_{\text{DEM}}(t) - \tau_{\text{model}}(t)]^2 \rangle}}{\sqrt{\langle \tau_{\text{DEM}}(t)^2 \rangle}}. \quad (\text{A2})$$

This last step leads to a refined estimation of the optimal triplet  $(\mu_D^{\text{opt}}, G_D^{\text{opt}}, G_E^{\text{opt}})$ . We provide in Fig. A3 the final value of the RMSE, defined in Eq. A2 and estimated at the optimal triplet, as a function of the dimensionless parameter  $\xi$  for all the data presented in this study. The model Eq. 4 reliably fits in the range of  $\xi \geq 0.1$  where the *linear* elasto-hysteretic regime prevails: the RMSE remains below 5%. However, the fits provides poorer results at low  $\xi$  where the *nonlinear* elastic contribution detailed in Sec. 4.5 becomes noticeable; in particular, the RMSE is larger than 10% for the three data introduced in Sec. 4.5 (see the white triangles at lowest  $\xi$ ), demonstrating the need to improve the model Eq. 4 as in Eq. 21.

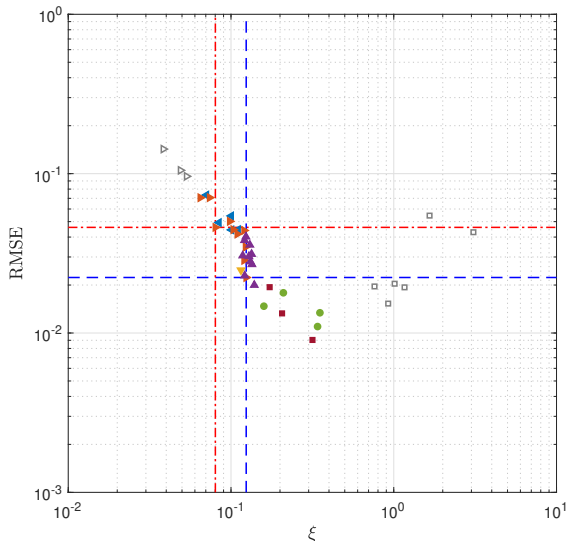


**Fig. A3** Optimal RMSE between stress-strain relation given by the elasto-hysteretic reduced model Eq. 4 and the simulations with DEM, as a function of the dimensionless parameter  $\xi$ . The red dashed-dotted line and the dashed blue line correspond to the computations from Figs. 1d and 1e at  $\gamma_m = 0.15$ , at  $\phi = 0.64$  and  $\phi = 0.70$ , respectively. The legend of the symbols is the same as in Fig. 6.

## Declarations

### Author Contributions

S.J. conducted the investigations. A.F. and S.J. did the investigations, prepared the figures, wrote and reviewed the manuscript. J.B., N.P. and J.L.D. discussed the results and reviewed the manuscript.

### Data availability

The authors declare that the data supporting the findings of this study are available within the paper itself. Raw data and computer codes are available from the corresponding author on reasonable request.

### Conflict of interest

The authors declare that they have no conflicts of interest to this work. They do not have any commercial or associative interest that represents a conflict of interest in connection with the work



submitted. The work described has not been submitted elsewhere for publication, in whole or in part, and all the authors listed have approved the manuscript that is enclosed.

## Funding

This study is based on the doctoral researches of the first author (A.F.) which were fully and equally funded by both our institutions, ISAE-Supméca and Estaca.

## Ethics approval and consent to participate

Not applicable

## References

- [1] H. M. Jaeger, S. R. Nagel, and R. P. Behringer. Granular solids, liquids, and gases. *Rev. Mod. Phys.*, 68(4):1259–1273, 1996. doi:[10.1103/revmodphys.68.1259](https://doi.org/10.1103/revmodphys.68.1259).
- [2] F. Melo, S. Job, F. Santibanez, and F. Tapia. Experimental evidence of shock mitigation in a hertzian tapered chain. *Phys. Rev. E*, 73(4):041305, 2006. doi:[10.1103/PhysRevE.73.041305](https://doi.org/10.1103/PhysRevE.73.041305).
- [3] M. Masmoudi, S. Job, M. S. Abbes, I. Tawfiq, and M. Haddar. Experimental and numerical investigations of dissipation mechanisms in particle dampers. *Granul. Matter*, 18(3):71, 2016. doi:[10.1007/s10035-016-0667-4](https://doi.org/10.1007/s10035-016-0667-4).
- [4] C. Hentati, S. Job, J.-Ph. Crété, M. Taktak, M. Haddar, and N. Dauchez. On the contact law of open-cell poro-granular materials. *Int. J. Solids Struct.*, 208-209:83–92, 2021. doi:[10.1016/j.ijsolstr.2020.10.023](https://doi.org/10.1016/j.ijsolstr.2020.10.023).
- [5] P. A. Johnson and X. Jia. Nonlinear dynamics, granular media and dynamic earthquake triggering. *Nature*, 437(7060):871–874, 2005. doi:[10.1038/nature04015](https://doi.org/10.1038/nature04015).
- [6] X. Jia, T. Brunet, and J. Laurent. Elastic weakening of a dense granular pack by acoustic fluidization: Slipping, compaction, and aging. *Phys. Rev. E*, 84(2):020301(R), 2011. doi:[10.1103/physreve.84.020301](https://doi.org/10.1103/physreve.84.020301).
- [7] R. Zuñiga, G. Varas, and S. Job. Geometry-controlled phase transition in vibrated granular media. *Sci. Rep.*, 12(1):14989, 2022. doi:[10.1038/s41598-022-18965-4](https://doi.org/10.1038/s41598-022-18965-4).
- [8] J. Ren, J. A. Dijkstra, and R. P. Behringer. Reynolds pressure and relaxation in a sheared granular system. *Phys. Rev. Lett.*, 110(1):018302, 2013. doi:[10.1103/physrevlett.110.018302](https://doi.org/10.1103/physrevlett.110.018302).
- [9] D. Espíndola, B. Galaz, and F. Melo. Creep of sound paths in consolidated granular material detected through coda wave interferometry. *Phys. Rev. E*, 94(1):012901, 2016. doi:[10.1103/PhysRevE.94.012901](https://doi.org/10.1103/PhysRevE.94.012901).
- [10] H. Götz and T. Pöschel. Granular meta-material: response of a bending beam. *Granul. Matter*, 25(3):58, 2023. doi:[10.1007/s10035-023-01336-9](https://doi.org/10.1007/s10035-023-01336-9).
- [11] C. Vasconcellos, R. Zuñiga, S. Job, and F. Melo. Localized energy absorbers in hertzian chains. *Phys. Rev. Appl.*, 18:014078, 2022. doi:[10.1103/PhysRevApplied.18.014078](https://doi.org/10.1103/PhysRevApplied.18.014078).
- [12] C. Vasconcellos, S. Job, and F. Melo. One-dimensional stepped chain of beads as a broadband acoustic diode. *Nonlinear Dyn.*, 2024. doi:[10.48550/arXiv.2408.09551](https://doi.org/10.48550/arXiv.2408.09551).
- [13] K. Walton. The effective elastic moduli of a random packing of spheres. *J. Mech. Phys. Solids*, 35(2):213–226, 1987. doi:[10.1016/0022-5096\(87\)90036-6](https://doi.org/10.1016/0022-5096(87)90036-6).
- [14] K. L. Johnson. *Contact Mechanics*. Cambridge University Press, Cambridge, 1985. doi:[10.1017/cbo9781139171731](https://doi.org/10.1017/cbo9781139171731).
- [15] V. L. Popov. *Contact Mechanics and Friction*. Springer Berlin, Heidelberg, 2010. doi:[10.1007/978-3-642-10803-7](https://doi.org/10.1007/978-3-642-10803-7).
- [16] GDR MiDi. On dense granular flows. *Eur. Phys. J. E*, 14(4):341–365, 2004. doi:[10.1140/epje/i2003-10153-0](https://doi.org/10.1140/epje/i2003-10153-0).
- [17] P. G. Rognon, J.-N. Roux, M. Naaim, and F. Chevoir. Dense flows of cohesive granular

- materials. *J. Fluid Mech.*, 596:21–47, 2008. doi:[10.1017/S0022112007009329](https://doi.org/10.1017/S0022112007009329).
- [18] P. Jop. Rheological properties of dense granular flows. *C. R. Phys.*, 16(1):62–72, 2015. doi:[10.1016/j.crhy.2014.12.001](https://doi.org/10.1016/j.crhy.2014.12.001).
- [19] A. Fall, M. Badetti, G. Ovarlez, F. Chevoir, and J.-N. Roux. Dry granular flows – Rheological measurements of the  $\mu(I)$ -rheology. *EPJ Web Conf.*, 140:03005, 2017. doi:[10.1051/epjconf/201714003005](https://doi.org/10.1051/epjconf/201714003005).
- [20] F. Da Cruz, S. Emam, M. Prochnow, J.-N. Roux, and F. Chevoir. Rheophysics of dense granular materials: Discrete simulation of plane shear flows. *Phys. Rev. E*, 72(2):021309, 2005. doi:[10.1103/physreve.72.021309](https://doi.org/10.1103/physreve.72.021309).
- [21] P. Jop, Y. Forterre, and O. Pouliquen. A constitutive law for dense granular flows. *Nature*, 441(7094):727–730, 2006. doi:[10.1038/nature04801](https://doi.org/10.1038/nature04801).
- [22] S. McNamara and W. R. Young. Inelastic collapse and clumping in a one-dimensional granular medium. *Phys. Fluids A*, 4(3):496–504, 1992. doi:[10.1063/1.858323](https://doi.org/10.1063/1.858323).
- [23] F. Pacheco-Vázquez and S. Dorbolo. Rebound of a confined granular material: combination of a bouncing ball and a granular damper. *Sci. Rep.*, 3(1):2158, 2013. doi:[10.1038/srep02158](https://doi.org/10.1038/srep02158).
- [24] M. Sánchez, G. Rosenthal, and L. A. Pugnaloni. Universal response of optimal granular damping devices. *J. Sound Vib.*, 331(20):4389–4394, 2012. doi:[10.1016/j.jsv.2012.05.001](https://doi.org/10.1016/j.jsv.2012.05.001).
- [25] G. Michon, A. Almajid, and G. Aridon. Soft hollow particle damping identification in honeycomb structures. *J. Sound Vib.*, 332(3):536–544, 2013. doi:[10.1016/j.jsv.2012.09.024](https://doi.org/10.1016/j.jsv.2012.09.024).
- [26] M. V. Ferreyra, M. Baldini, L. A. Pugnaloni, and S. Job. Effect of lateral confinement on the apparent mass of granular dampers. *Granul. Matter*, 23(2):45, 2021. doi:[10.1007/s10035-021-01090-w](https://doi.org/10.1007/s10035-021-01090-w).
- [27] E. Kausel and D. Assimaki. Seismic simulation of inelastic soils via frequency-dependent moduli and damping. *J. Eng. Mech-asc.*, 128:34–47, 2002. URL <https://api.semanticscholar.org/CorpusID:85507801>.
- [28] L. Rouleau. *Modélisation vibro-acoustique de structures sandwich munies de matériaux visco-élastiques*. PhD thesis, Conservatoire national des arts et métiers - CNAM, 2013. URL <https://theses.hal.science/tel-00957457>.
- [29] D. Bi, J. Zhang, B. Chakraborty, and R. P. Behringer. Jamming by shear. *Nature*, 480(7377):355–358, 2011. doi:[10.1038/nature10667](https://doi.org/10.1038/nature10667).
- [30] D. Assimaki, E. Kausel, and A. Whittle. Model for dynamic shear modulus and damping for granular soils. *J. Geotech. Geoenviron.*, 126(10):859–869, 2000. doi:[10.1061/\(asce\)1090-0241\(2000\)126:10\(859\)](https://doi.org/10.1061/(asce)1090-0241(2000)126:10(859)).
- [31] H. G. Brandes. Simple shear behavior of calcareous and quartz sands. *Geotech. Geol. Eng.*, 29(1):113–126, 2010. doi:[10.1007/s10706-010-9357-x](https://doi.org/10.1007/s10706-010-9357-x).
- [32] K. Senetakis, A. Anastasiadis, and K. Pitilakis. Normalized shear modulus reduction and damping ratio curves of quartz sand and rhyolitic crushed rock. *Soils Found.*, 53(6):879–893, 2013. doi:[10.1016/j.sandf.2013.10.007](https://doi.org/10.1016/j.sandf.2013.10.007).
- [33] A. Awdi, C. Chateau, F. Chevoir, J.-N. Roux, and A. Fall. Viscous dissipation in large amplitude oscillatory shear of unsaturated wet granular matter. *J. Rheol.*, 67(2):365–372, 2023. doi:[10.1122/8.0000507](https://doi.org/10.1122/8.0000507).
- [34] Y. Xing, J. Zheng, J. Li, Y. Cao, W. Pan, J. Zhang, and Y. Wang. X-ray tomography investigation of cyclically sheared granular materials. *Phys. Rev. Lett.*, 126(4):048002, 2021. doi:[10.1103/physrevlett.126.048002](https://doi.org/10.1103/physrevlett.126.048002).
- [35] M. H. Khalili, J.-N. Roux, J.-M. Pereira, S. Brisard, and M. Bornert. Numerical study of one-dimensional compression of granular materials. i. stress-strain behavior,

- microstructure, and irreversibility. *Phys. Rev. E*, 95:032907, 2017. doi:[10.1103/PhysRevE.95.032907](https://doi.org/10.1103/PhysRevE.95.032907).
- [36] M. H. Khalili, J.-N. Roux, J.-M. Pereira, S. Brisard, and M. Bornert. Numerical study of one-dimensional compression of granular materials. ii. elastic moduli, stresses, and microstructure. *Phys. Rev. E*, 95:032908, 2017. doi:[10.1103/PhysRevE.95.032908](https://doi.org/10.1103/PhysRevE.95.032908).
- [37] T. G. Sitharam and J. S. Vinod. Evaluation of shear modulus and damping ratio of granular materials using discrete element approach. *Geotech. Geol. Eng.*, 28(5):591–601, 2010. doi:[10.1007/s10706-010-9317-5](https://doi.org/10.1007/s10706-010-9317-5).
- [38] X. Zhong and W. Sun. An adaptive reduced-dimensional discrete element model for dynamic responses of granular materials with high frequency noises. *Int. J. Multiscale Com.*, 16(4):345–366, 2018. doi:[10.1615/intjmultcompeng.2018026895](https://doi.org/10.1615/intjmultcompeng.2018026895).
- [39] V. Magnanimo and S. Luding. A local constitutive model with anisotropy for ratcheting under 2d axial-symmetric isobaric deformation. *Granul. Matter*, 13(3):225–232, 2011. doi:[10.1007/s10035-011-0266-3](https://doi.org/10.1007/s10035-011-0266-3).
- [40] D. Krijgsman and S. Luding. 2d cyclic pure shear of granular materials, simulations and model. *AIP Conf. Proc.*, 1542(1):1226–1229, 2013.
- [41] Y. Jiang and M. Liu. Granular solid hydrodynamics. *Granul. Matter*, 11(3):139–156, 2009. doi:[10.1007/s10035-009-0137-3](https://doi.org/10.1007/s10035-009-0137-3).
- [42] G. Gudehus. Granular solid dynamics with eutaxy and hysteresis. *Acta Geotech.*, 15(5):1173–1187, 2019. doi:[10.1007/s11440-019-00820-y](https://doi.org/10.1007/s11440-019-00820-y).
- [43] J. M. Bajkowski, B. Dyniewicz, M. Gebik-Wrona, J. Bajkowski, and C. I. Bajer. Reduction of the vibration amplitudes of a harmonically excited sandwich beam with controllable core. *Mech. Syst. Signal Pr.*, 129:54–69, 2019. doi:[10.1016/j.ymsp.2019.04.024](https://doi.org/10.1016/j.ymsp.2019.04.024).
- [44] A. Fichant, J.-L. Dion, S. Job, and N. Peyret. Granular vibration damping kit equipping an equipment support, Patent FR3127997B1 (Safran Spacecraft Propulsion, France), 2024. URL <https://patents.google.com/patent/FR3127997B1/en>.
- [45] V. Šmilauer and *et al.* *Yade documentation*. The Yade Project, 2021. doi:[10.5281/zenodo.5705394](https://doi.org/10.5281/zenodo.5705394).
- [46] H. A. Makse, N. Gland, D. L. Johnson, and L. Schwartz. Granular packings: Nonlinear elasticity, sound propagation, and collective relaxation dynamics. *Phys. Rev. E*, 70(6):061302, 2004. doi:[10.1103/physreve.70.061302](https://doi.org/10.1103/physreve.70.061302).
- [47] C. Thornton. Numerical simulations of deviatoric shear deformation of granular media. *Géotechnique*, 50(1):43–53, 2000. doi:[10.1680/geot.2000.50.1.43](https://doi.org/10.1680/geot.2000.50.1.43).
- [48] C. S. O’Hern, L. E. Silbert, A. J. Liu, and S. R. Nagel. Jamming at zero temperature and zero applied stress: The epitome of disorder. *Phys. Rev. E*, 68(1):011306, 2003. doi:[10.1103/physreve.68.011306](https://doi.org/10.1103/physreve.68.011306).
- [49] A. Faulconnier. *Contrôle des vibrations de poutres par composites multicouches granulaires*. PhD thesis, Université Paris-Saclay, 2023. URL <https://theses.hal.science/tel-04622579>.
- [50] J.-N. Roux, M. H. Khalili, F. Froio, and C. Dequeker. Elasticity and mechanical behaviour of granular materials: Some insights from numerical studies of simple systems. In *Advances in Mechanics and Mathematics*, pages 185–224. Springer International Publishing, 2020. doi:[10.1007/978-3-030-49267-0\\_9](https://doi.org/10.1007/978-3-030-49267-0_9).
- [51] P. R. Dahl. A solid friction model. Technical report, Aerospace Corp (El Segundo, CA), 1968.
- [52] P. R. Dahl. Measurement of solid friction parameters of ball bearings. Technical report, Aerospace Corp (El Segundo, CA), 1977.

- [53] E. Piollet, D. Poquillon, and G. Michon. Dynamic hysteresis modelling of entangled cross-linked fibres in shear. *J. Sound Vib.*, 383:248–264, 2016. doi:[10.1016/j.jsv.2016.06.023](https://doi.org/10.1016/j.jsv.2016.06.023).
- [54] N. Peyret, M. Rosatello, G. Chevallier, and J.-L. Dion. A mindlin derived dahl friction model. *Mech. Mach. Theory*, 117:48–55, 2017. doi:[10.1016/j.mechmachtheory.2017.06.019](https://doi.org/10.1016/j.mechmachtheory.2017.06.019).
- [55] D. Helmick and W. Messner. Describing function analysis of dahl model friction. In *American Control Conference*. IEEE, 2009. doi:[10.1109/acc.2009.5159996](https://doi.org/10.1109/acc.2009.5159996).
- [56] A. Al Majid and R. Dufour. Harmonic response of a structure mounted on an isolator modelled with a hysteretic operator: experiments and prediction. *J. Sound Vib.*, 277(1-2):391–403, 2004. doi:[10.1016/j.jsv.2003.09.025](https://doi.org/10.1016/j.jsv.2003.09.025).
- [57] E. Delfosse-Ribay, I. Djeran-Maigre, R. Cabrillac, and D. Gouvenot. Shear modulus and damping ratio of grouted sand. *Soil Dyn. Earthq. Eng.*, 24(6):461–471, 2004. doi:[10.1016/j.soildyn.2004.02.004](https://doi.org/10.1016/j.soildyn.2004.02.004).
- [58] M. Badetti, A. Fall, F. Chevoir, and J.-N. Roux. Shear strength of wet granular materials: macroscopic cohesion and effective stress. *Eur. Phys. J. E*, 41:68, 2018. doi:[10.1140/epje/i2018-11677-8](https://doi.org/10.1140/epje/i2018-11677-8).